

Phosphorus Layers

mP-BaP₃: A New Phase from an Old Binary SystemJuli-Anna Dolyniuk,^[a] Derrick C. Kaseman,^[b] Sabyasachi Sen,^[b] Jing Zhao,^[a]
Frank E. Osterloh,^[a] and Kirill Kovnir*^[a]

Abstract: A polyphosphide, *mP*-BaP₃, with a unique two-dimensional phosphorus layer has been discovered and characterized. It crystallizes in the monoclinic space group *P*₂₁/*c* with unit-cell parameters *a* = 6.486(1), *b* = 7.710(1), *c* = 8.172(2) Å; β = 104.72(3)°; *Z* = 4. Its phosphorus polyanion can be derived from the strong elongation of 2/3 of the P–P bonds present in the layers of black phosphorus. The unit-cell volume of the *mP*-BaP₃ phase is 1.4% larger than the volume of another polymorph, *mS*-BaP₃, reported more than

40 years ago. The latter phase features the presence of one-dimensional phosphorus chains separated by Ba atoms. The differences in the structures of the phosphorus fragments in both polymorphs of barium triphosphide result in large differences in both the thermal stability of these materials as well as in their properties as evidenced by DSC, ³¹P solid-state MAS NMR, UV/Vis, and surface photovoltage spectroscopies, alongside quantum-chemical calculations.

Introduction

Metal polyphosphides are a highly explored topic of interest in inorganic chemistry since they exhibit unique structural features and a range of appealing properties from magnetism to thermoelectricity.^[1,2] Similar to carbon, phosphorus atoms form well-ordered rings, chains, tubes, and sheets that can be integrated to form complex phosphorus backbones.^[1–12] Unlike carbon, however, phosphorus atoms are only able to form one, two, and three homoatomic bonds to each other as opposed to the commonly found four-bonded carbon atoms. This leads to the P^{2–}, P^{1–}, and P⁰ oxidation states, respectively.

Based on current knowledge, barium forms ten structurally characterized polyphosphides with different phosphorus to barium ratios: Ba₃P₂ (0.67),^[13] Ba₄P₃ (0.75),^[14] Ba₅P₄ (0.8),^[15] Ba₃P₄ (1.3),^[16] Ba₅P₉ (1.8),^[7] BaP₂ (2),^[1,17] BaP₃ (3),^[18] Ba₃P₁₄ (4.7),^[19] BaP₈ (8),^[8] and BaP₁₀ (10).^[20] BaP₃ along with the other binaries are common byproducts in the syntheses of ternary P-rich barium polyphosphides. During our exploration of the ternary Ba–Au–P system,^[21,22] we identified a new barium polyphosphide with the composition BaP₃ and the Pearson symbol *mP*16. This phase is quite different from the originally discovered polymorph, a BaP₃ phase with the Pearson symbol *mS*16, discovered by von Schnering and Dahlmann more than 40 years

ago.^[18] To distinguish between these two modifications, we will use a derivative of the structures' Pearson symbols throughout the manuscript: *mS*-BaP₃ for the original modification and *mP*-BaP₃ for the newly discovered phase.

mP-BaP₃ crystallizes into a new phosphide structure type, which is different from other known binary pnictides. We characterized the *mP*-BaP₃ phase and, for comparison, the *mS*-BaP₃ phase by using powder and single-crystal X-ray diffraction, energy-dispersive X-ray spectroscopy (EDX), differential scanning calorimetry (DSC), UV/Vis spectroscopy, surface photovoltage spectroscopy (SPS), solid-state ³¹P NMR spectroscopy, and quantum-chemical calculations that included electron localization function (ELF) analysis.

Results and Discussion

Synthesis

The *mP*-BaP₃ phase was first observed during an exploration of the ternary Ba–Au–P system.^[21,22] A synthesis in molten tin flux at 1073 K resulted in the formation of dark-red crystals of *mP*-BaP₃. Attempts to recreate this phase from elements at 1073 K resulted in nearly single-phase samples. We also verified the findings of von Schnering and Dahlmann, who previously synthesized *mS*-BaP₃ by either high-temperature reactions (1373 K) or by using sulfur as a transport agent.^[18] We confirm that *mS*-BaP₃ can indeed be produced either from the reactions of elements at temperatures above 1150 K or by the use of small amounts of iodine as a transport agent. In the latter case, *mS*-BaP₃ formed at temperatures as low as 1073 K. However, iodine proved to be very reactive, and the reactions with more than a few crystals of I₂ led to the formation of Ba₂P₇I.^[23] To clarify the *mS*/*mP* phase relationship, we per-

[a] J.-A. Dolyniuk, J. Zhao, Prof. Dr. F. E. Osterloh, Prof. Dr. K. Kovnir
Department of Chemistry, University of California, Davis
One Shields Avenue, Davis, CA 95616 (USA)
E-mail: kkovnir@ucdavis.edu

[b] D. C. Kaseman, Prof. Dr. S. Sen
Department of Chemical Engineering and Materials Science
University of California, Davis
One Shields Avenue, Davis, CA 95616 (USA)

Supporting information for this article is available on the WWW under
<http://dx.doi.org/10.1002/chem.201305078>.

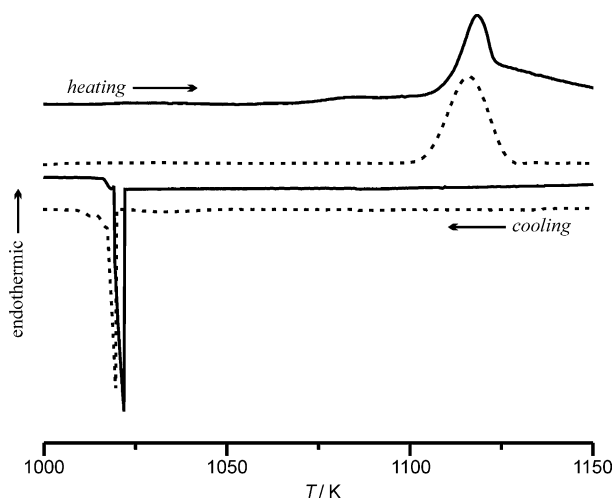


Figure 1. Differential scanning calorimetry plot of *mS*-BaP₃ and *mP*-BaP₃. Broad melting peaks are observed upon heating, while sharp crystallization peaks are observed upon cooling (—: *mS*-BaP₃; - - - -: *mP*-BaP₃).

formed differential scanning calorimetry (DSC) characterizations of BaP₃ samples (Figure 1).

The DSC curves for both *mP*-BaP₃ and *mS*-BaP₃ are similar over the studied temperature range. Both modifications of BaP₃ have similar melting offset temperatures at 1105(3) (*mP*-BaP₃) and 1109(3) K (*mS*-BaP₃). Both melts crystallize at similar temperatures: 1020(3) (*mP*-BaP₃) and 1022(3) K (*mS*-BaP₃). Powder X-ray diffraction of *mS*- and *mP*-BaP₃ samples after DSC experiments show in all cases the formation of only *mS*-BaP₃ upon crystallization of the melts. This explains why reactions at temperatures above the melting temperature resulted in the formation of solely *mS*-BaP₃.

To confirm DSC results, we performed a series of subsequent annealings. The results are summarized in Figure 2. Annealing or re-annealing either of the *mP*-BaP₃ or *mS*-BaP₃ phases at 1073 K for 140 h led to the formation of the *mP*-BaP₃ phase. Heating either sample above the melting point resulted in the formation of the *mS*-BaP₃ phase. Based on both the results of our syntheses and DSC experiments we hypothesize that *mS*-BaP₃ is the high-temperature thermodynamically stable phase, whereas *mP*-BaP₃ is the low-temperature thermodynamically stable phase. The transformation of *mS*-BaP₃ into *mP*-BaP₃ by low-temperature annealing rules out the metastable nature of *mP*-BaP₃.

Our synthetic results indicate that the phase relationship in this system is sensitive to the pressure of gaseous components in the reaction ampoule. As was

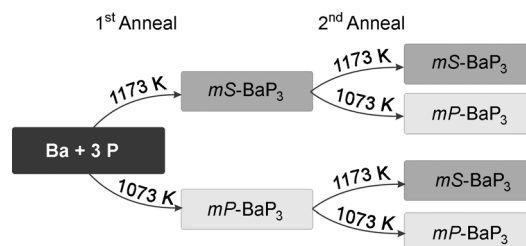


Figure 2. BaP₃ synthesis scheme. Syntheses at 1073 K (below the melting point) led to the formation of *mP*-BaP₃, whereas syntheses at 1173 K (above the melting point) led to the formation of *mS*-BaP₃.

revealed by single-crystal X-ray diffraction, *mP*-BaP₃ has a larger volume (395.3 Å³) than *mS*-BaP₃ (389.6 Å³); the difference is 1.4%. It is probable that a higher pressure would favor the formation of the lower volume phase, *mS*-BaP₃. More detailed studies of the pressure-structure relationships for the BaP₃ polyphosphides are out of scope of this work and will be reported elsewhere.

Crystal structure

Polyphosphides composed of like or similar cations are known to display a variety of crystal structure types. It is not uncommon for binary polyphosphides to have two different polymorphic modifications, often referred to as the α and β phases. These are known for both SrP₃ and EuP₃ of the triphosphide family as well as for many other polyphosphides, including some of the M₃P₇,^[1,24] M₄P₆,^[1,25] and M₃P₁₁^[1,26] families (M = Na–Cs).

In the crystal structure of elemental black phosphorus (Figure 3, top) all P atoms are 3-bonded, forming a puckered layer of condensed P₆ rings in chair conformation. Each P atom

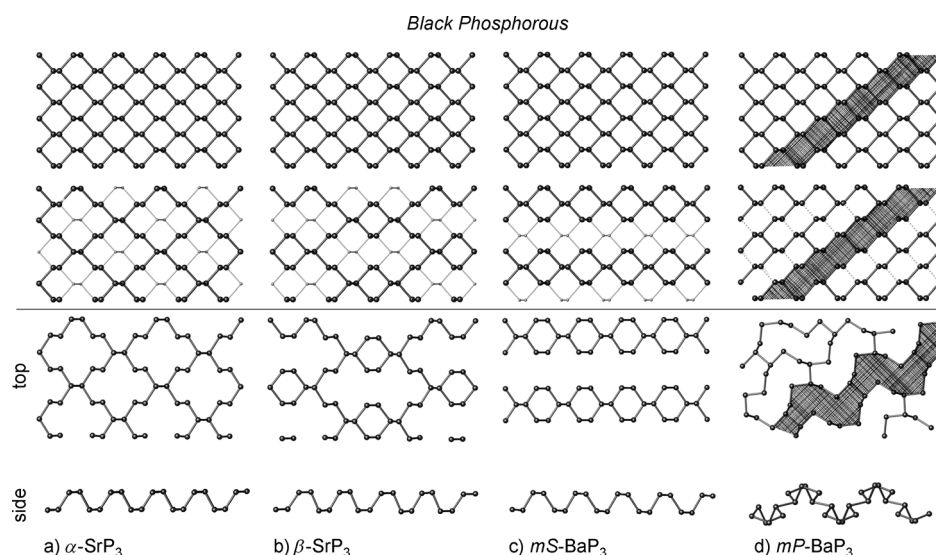


Figure 3. Two top panels: phosphorus layer in the crystal structure of black phosphorus, in the second row different atoms or bonds are shadowed to show relation to the layers of corresponding phosphides. Two bottom panels: top and side view of the phosphorus layer in the crystal structure of binary phosphides MP₃ (M = Ca–Ba, Eu). Shown from left to right are structure types of a) α -SrP₃,^[8] b) β -SrP₃,^[19] c) *mS*-BaP₃,^[18] and d) the new *mP*-BaP₃ phase (current work).

utilizes three electrons to form three covalent bonds, and maintains a leftover electron lone pair, making it formally a P^0 atom. In the crystal structure of all MP_3 polyphosphides ($M = Ca, Sr, Ba, Eu$), the metal atoms bear a +2 positive charge, whereas the phosphorus polyanion has a -2 negative charge, P_3^{2-} . Two-bonded phosphorus atoms with two electron lone pairs are formally P^{1-} . Thus, in the crystal structure of MP_3 , the two- and three-bonded P atoms ratio is 2:1.

Each MP_3 structure can be derived from the crystal structure of black phosphorus. Three previously reported P_3^{2-} phosphorus polyanions present in the MP_3 structures can be formed by the removal of some of the phosphorus atoms from the black phosphorus layers. Such atoms are shadowed in the second row of Figure 3. This results in the formation of either P layers in the cases of Sr-, Eu-, and Ca-containing phases (Figures 3a and 3b) or P chains in the case of $mS-BaP_3$ (Figure 3c). The α - SrP_3 -types, adopted by α - SrP_3 ,^[6] α - EuP_3 ,^[11] and CaP_3 ,^[12] are composed of 14-membered rings that are formed upon the elimination of next-neighbor pairs of P atoms from the black phosphorus layer. The β - SrP_3 type is also adopted by β - EuP_3 and has both six- and 22-membered rings that are formed when adjacent pairs of P atoms are removed from the black P layer.^[1,19] The BaP_3 phases are structurally unique compounds among the binary MP_3 structures. $mS-BaP_3$ can be derived from black P by the removal of full rows of P atoms to form chains of linked six-membered rings.^[18]

To derive the structure of the $mP-BaP_3$ no removal of P atoms from the black phosphorus layer is necessary. Instead, the significant elongation of 2/3 of the P–P distances (----- in Figure 3d, middle) is required, resulting in a significant distortion of the layer (Figure 3d, bottom). This leads to the formation of sheets of 14-membered phosphorus rings, in chair configurations, with barium atoms sandwiched between the sheets. A similar route can be proposed for the description of the phosphorus polyanion in the CdP_4 polyphosphide.^[27] The composition for the latter compound can be written as $(Cd^{2+})(P_4^{2-})$. Thus, the ratio of the three- and two-bonded P atoms is 1:1. To produce the phosphorus polyanion present in the crystal structure of CdP_4 , half of all P–P bonds in black phosphorus layer need to be elongated, resulting in the formation of puckered 10-membered rings (Figure 4c–d). In turn, in $mP-BaP_3$, 2/3 of all P–P bonds get elongated, thus resulting in 14-membered rings. In the crystal structure of $mP-BaP_3$ phosphorus layers are situated on top of each other, stacked along the [100] direction (Figure 4a–b).

The Ba atoms of both BaP_3 phases have in total 10 nearest-neighbor phosphorus atoms (Figure 5a). In $mP-BaP_3$ and $mS-BaP_3$, the barium coordination polyhedra have a four-membered phosphorus base, and distorted, capped five-membered phosphorus rings on top. The mirror plane present in $mS-BaP_3$ leads to more symmetrical polyhedra. The shortest Ba–P distances (3.25 Å) in $mP-BaP_3$ are longer than those distances in $mS-BaP_3$ (3.21 Å). The closest Ba–Ba distances in these phases also increase drastically from 3.97 for $mS-BaP_3$ to 4.52 Å for $mP-BaP_3$. This difference in nonbonding interatomic distances aligns with the observed unit-cell volume difference for the two phases. If the shortest Ba–P distances are taken into ac-

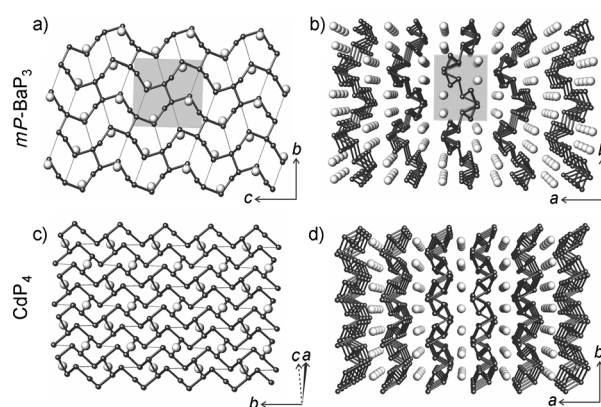


Figure 4. Top: the crystal structure of $mP-BaP_3$: a) single layer and b) general view along the [001] direction. Bottom: the crystal structure of CdP_4 : c) single layer and d) general view along the [001] direction. ----- represents the proposed broken P–P bonds, and they are omitted in (b) and (d) for clarity. P: black; Ba/Cd: white. Unit cell is shown as a grey rectangle.

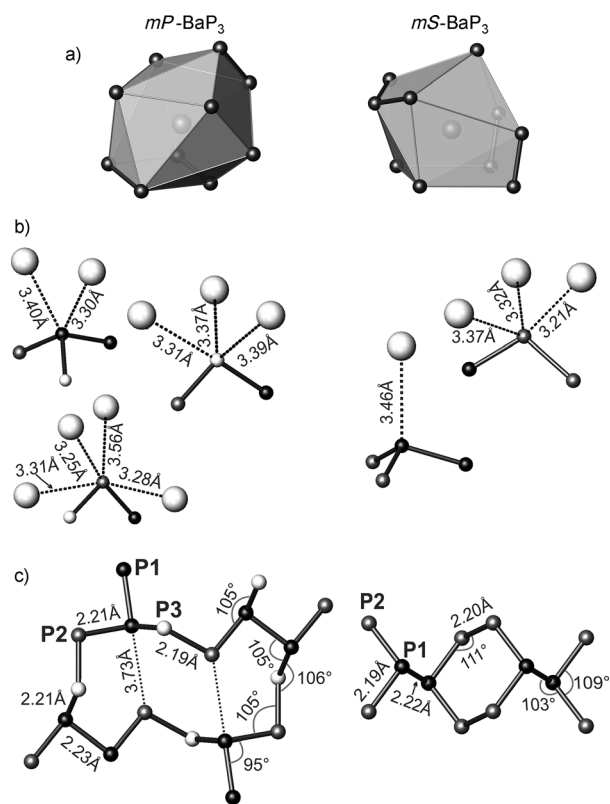


Figure 5. Comparison of the local coordination of $mP-BaP_3$ (left) and $mS-BaP_3$ (right): a) Ba coordination; b) phosphorus coordination with shortest Ba–P distances; c) bond length and angles in the polyphosphide fragments. The dashed lines represent the proposed elongated distances in $mP-BaP_3$. In (b) and (c) P1: small black; P2: small grey; P3: small white; Ba: large white.

count, the local coordination of P atoms is different in each of the two modifications of BaP_3 (Figure 5b). Despite the observed difference in the unit-cell volume, P–P distances are similar in both modifications of BaP_3 , ranging from 2.19 to 2.23 Å (Figure 5c). These distances are within the normal single P–P bond ranges present in other polyphosphides.^[1,2] In the

puckered phosphorus layers of mP -BaP₃, significant deviations from ideal tetrahedral angles are found, for example $\angle P1-P1-P2$ is 95°, whereas in the structure of mS -BaP₃ all angles are close to an ideal tetrahedral angle (Figure 5c).

³¹P solid-state magic-angle spinning NMR spectroscopy (MAS-NMR)

The ³¹P MAS NMR spectra of mS -BaP₃ and mP -BaP₃ phases are shown in Figure 6. These spectra clearly show the presence of two and three distinct P environments in mS -BaP₃ and mP -BaP₃, respectively. This is consistent with the crystal structures determined from X-ray diffraction experiments. The sideband patterns in these ³¹P MAS spectra collected at different spinning speeds were simulated by using the Herzfeld–Berger method with the software package DMFit^[28] to obtain the chemical shift anisotropy (CSA) and the asymmetry parameter

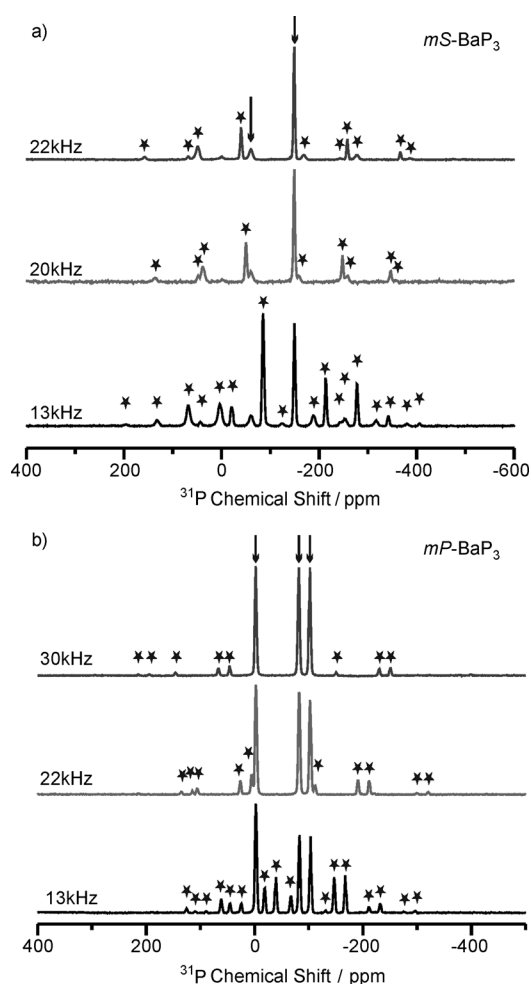


Figure 6. ³¹P MAS NMR spectra of a) mS -BaP₃ and b) mP -BaP₃ collected at different spinning speeds (denoted alongside each spectrum). The spinning sidebands are denoted by the asterisks. mS -BaP₃: peaks at -60 and -149 ppm (shown with arrows) correspond to the isotropic shifts of P1 and P2 sites, respectively. mP -BaP₃: peaks at -3 , -82 , and -103 ppm (shown with arrows) correspond to the isotropic shifts of P1, P3, and P2 sites, respectively.

Phase	³¹ P isotropic shift [ppm]	CSA [ppm]	Asymmetry parameter η_{CS}	Assignment
mS -BaP ₃	-60	-350	0.03	P1
	-149	-180	0.60	P2
mP -BaP ₃	-3	85	0.52	P1
	-82	136	0.67	P3
	-103	-136	0.89	P2

η_{CS} for each site. These parameters for each isotropic ³¹P NMR spectroscopic peak are listed in Table 1.

In the case of mS -BaP₃, the two ³¹P isotropic shifts are located at -60 and -149 ppm, and integration of these isotropic peaks and their corresponding spinning sidebands yields a ratio of $\sim 1:2$ that allows for unequivocal assignment of these peaks to the P1 and P2 crystallographic sites, respectively. The ³¹P isotropic chemical shift of the twofold coordinated P2 site is within the range characteristic of P atoms with formal negative charge P^{1-} .^[29] The larger shielding of the P2 site compared to the threefold coordinated P1 site indicates the presence of Ba nearest neighbors plays an important role in controlling the chemical shifts of the phosphorus sites in these materials. The three Ba nearest neighbors of the P2 site are consistent with a larger shielding relative to the P1 site with only one Ba nearest neighbor. It is also interesting to note the extremely large CSA (-350 ppm) and small η_{CS} value for the P1 site (Table 1). This result is in fact consistent with the distorted tetrahedral geometry of the nearest-neighbor coordination polyhedron for this site (close to $3m$ local symmetry) that consists of 3P and 1Ba atoms at the corners of the tetrahedron (Figure 5). The tetrahedron is significantly elongated along the unique direction of the Ba–P bond that defines the uniaxial symmetry for the P1 site, manifested in the near-zero value of η_{CS} . The substantial distortion of the tetrahedron, on the other hand, corresponds to the large CSA of this site.

The ³¹P MAS NMR spectra of mP -BaP₃ show three peaks in a 1:1:1 ratio with isotropic shifts of -3 , -82 , and -103 ppm, again completely consistent with the three expected crystallographic P sites, P1, P2, and P3 at a 1:1:1 ratio (Figure 5b). The equal ratio of the 3 sites makes ³¹P NMR peak assignment somewhat challenging for this phase. Following the assignment of the most-shielded ³¹P peaks to the formally negatively charged phosphorus sites in mS -BaP₃, one can readily assign the peaks at -103 and -82 ppm to the two P^{1-} sites, P2 and P3. The P2 site has 3 Ba nearest neighbors at an average distance of 3.28 Å and 1 Ba at 3.56 Å, whereas the P3 site has 3 Ba nearest neighbors at an average distance of 3.35 Å (Figure 5b). The higher number of Ba nearest neighbors and the shorter average Ba–P distance for the 3 nearest neighbors for the P2 site are expected to give rise to stronger shielding for the P2 site relative to that for the P3 site. Therefore, we assign the peaks at -103 and -82 ppm to the P2 and P3 sites in mP -BaP₃, respectively. Finally, the peak with ³¹P isotropic shift at -3 ppm can be assigned to the P1 site in mP -BaP₃. The significant downfield shift (i.e. deshielding) of the position of this

peak compared to that (−60 ppm) observed for the three-bonded P1 site in *mS*-BaP₃ may be related to the substantially smaller \angle P1-P1-P2 bond angles in *mP*-BaP₃ (Figure 5c).

Electronic structure

MP₃ polyphosphides are typical Zintl phases^[30,31] with compositions written as (M²⁺)(P⁰)₁(P¹⁻)₂. The results of band-structure calculations confirm that both BaP₃ phases are semiconducting Zintl phases (Figure 7). In agreement with the assumptions

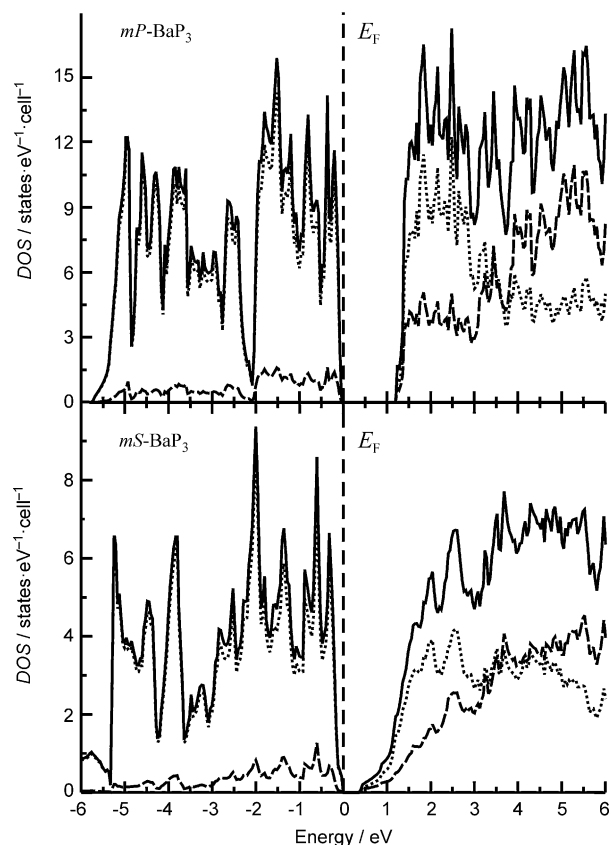


Figure 7. Density of states (DOS) diagram for *mP*-BaP₃ (top) and *mS*-BaP₃ (bottom). Contributions from Ba and P orbitals are shown as ----- and, respectively; — shows the total contribution.

drawn from applying the Zintl concept, the top of the valence band is comprised of P orbitals with small contributions from Ba orbitals, whereas the bottom of the conduction band has a significant contribution from Ba orbitals. Nonbonding Ba–P separations are an essential factor in the widths of the band gap. In *mS*-BaP₃, phosphorus and barium atoms are closer to each other than they are in *mP*-BaP₃ (Figure 5), which should lead to a narrower bandgap. The calculated bandgaps agree with this assumption. The FPLO full potential calculations predict substantially different bandgaps for the two polymorphic modifications of BaP₃: 1.2 eV for *mP*-BaP₃ and 0.4 eV for *mS*-BaP₃. Another calculation method, LMTO, predicts a similar difference: 1.5 eV for *mP*-BaP₃ and 0.5 eV for *mS*-BaP₃ (Table 2).

	<i>mP</i> -BaP ₃	<i>mS</i> -BaP ₃
color	deep red	black
E_g calculated—FPLO [eV]	1.2	0.4
E_g calculated—LMTO [eV]	1.5	0.5
E_g KM diffuse reflectance [eV]	1.5	< 1.2
E_g SPS [eV]	> 0.7	> 0.7

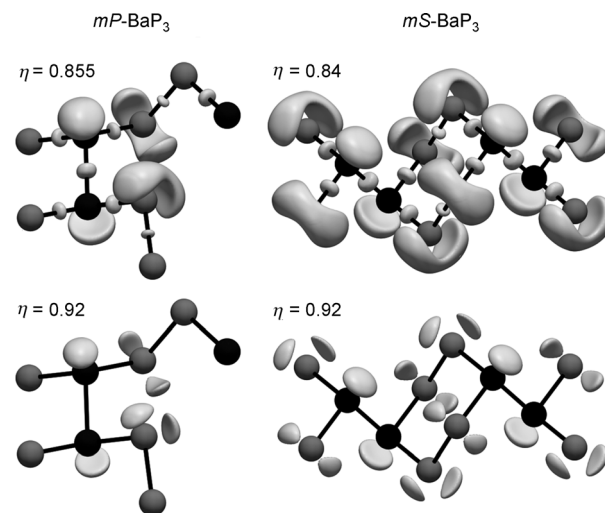


Figure 8. 3D isosurfaces of electron localization function (η) for the fragments of phosphorus polyanions in *mP*-BaP₃ (left) and *mS*-BaP₃ (right). Three-coordinated phosphorus atoms: black; two-coordinated phosphorus atoms: grey.

To clarify the bonding in the phosphorus polyanions in both modifications of BaP₃, we applied electron localization function (ELF) analysis (Figure 8). The observed distribution of the localized electrons is in agreement with the predictions of the Zintl concept. One and two electron lone pairs are expected to be located on the two- and three-bonded phosphorus atoms, respectively, and single covalent bonds are expected to be present at short P–P interatomic separations. The ELF analysis indicates the presence of the expected number of electron lone pairs (Figure 8, bottom). In both types of the P₃²⁻ polyanions the two bonded phosphorus atoms (grey) have two electron lone pairs, whereas the three-bonded ones (black) have only one electron lone pair. Localization domains corresponding to the covalent two-centered P–P interactions were found for all of the short interatomic separations (Figure 8, top). Despite some deviations of the angles in the layered P₃²⁻ found in *mP*-BaP₃ from regular tetrahedral angles, no displacement of the ELF maxima from the line connecting atoms was observed. This is in contrast to the more strained isolated polyphosphide cage, P₇³⁻, found in Ba₂P₇I in which ELF maxima are shifted from the edges of the base triangle.^[23] The observed ELF distribution allows for the qualification of both *mS*-BaP₃ and *mP*-BaP₃ as classical Zintl phases. No ELF maxima were detected near the shortest Ba–P separations, which are indicated by ----- in Figure 5b.

Kubelka–Munk diffuse reflectance and surface photovoltage spectroscopy (SPS)

All attempts to measure resistivity of both modifications of BaP_3 were unsuccessful. We were not able to grow large enough crystals for the measurements. The sintering of pressed pellets resulted in changes of the composition of the pellets, probably due to the evaporation of small amounts of phosphorus. Therefore, Kubelka–Munk (KM) diffuse reflectance measurements^[32,33] were utilized to determine the bandgaps of $mP\text{-BaP}_3$ and $mS\text{-BaP}_3$. Based on its black color and the results of theoretical calculations, $mS\text{-BaP}_3$ is expected to have a bandgap below 1.0 eV. Indeed, preliminary diffuse reflectance measurements showed the bandgap for $mS\text{-BaP}_3$ to be smaller than 1.2 eV, the instrument limit. In the case of $mP\text{-BaP}_3$, there was a strong KM diffuse reflectance signal, and an approximation of the indirect bandgap from this data was on par with the calculated bandgap (Figure 9, Table 2) as well as with the observed deep-red color of the $mP\text{-BaP}_3$ crystals.

To further characterize the electronic properties of BaP_3 , surface photovoltage spectroscopy (SPS) was employed. In SPS, the contact potential difference (CPD) of an illuminated sample is measured contactless with a gold Kelvin probe as a function of photon energy. This provides information about band gaps, defects, carrier type, and energetics of the sample material.^[34–40] Surface photovoltage spectra for $mP\text{-BaP}_3$ and $mS\text{-BaP}_3$ films are shown in Figure 10 together with the spectrum of a reference material, PbS. $mP\text{-BaP}_3$ exhibits a photovoltage signal with an onset of 0.8 eV and reaches a maximum of -0.6 V at 1.8 eV. The negative voltage sign indicates the movement of electron carriers towards the gold substrate, as is often seen with n -type semiconductors.^[36,37] The spectrum for $mS\text{-BaP}_3$ has a much lower photovoltage of only -0.1 V at 1.6 eV, with an apparent onset near 1.0 eV. Careful inspection of the SPS spectra reveals (inset in Figure 10) the true onset occurs at 0.8 eV, close to that of $mP\text{-BaP}_3$. The similar photo-onsets for both BaP_3 samples do not agree with the optical and theoretical data, which indicate that the bandgap of $mS\text{-BaP}_3$ should be significantly smaller than the bandgap of $mP\text{-BaP}_3$. The discrepancy could be due to the presence of mid-gap defect states on the surface of the $mP\text{-BaP}_3$ crystals, which produce charge carriers under infrared-light excitation. Because SPS measures voltage, not current, it is sensitive to even small changes in the charge distribution that result from excitation of defects.^[40] For reference, the spectrum of a PbS film was also recorded, and the onset was found to be at 0.55 eV, approximately 0.1 eV higher than the reported bandgap of 0.41–0.42 eV.^[41,42] Based on the reference measurement and assuming similar accuracy of 0.1 eV, the lower limit for the bandgap of both modifications of BaP_3 can be estimated as $0.8 - 0.1 = 0.7$ eV. Summarizing the results of two optical methods, diffuse reflectance and SPS, the bandgap of $mS\text{-BaP}_3$ is predicted to be in the range of 0.7–1.2 eV (Table 2). Band structure calculations suggested a smaller bandgap, which is expected, since calculations are known to underestimate the bandgap.

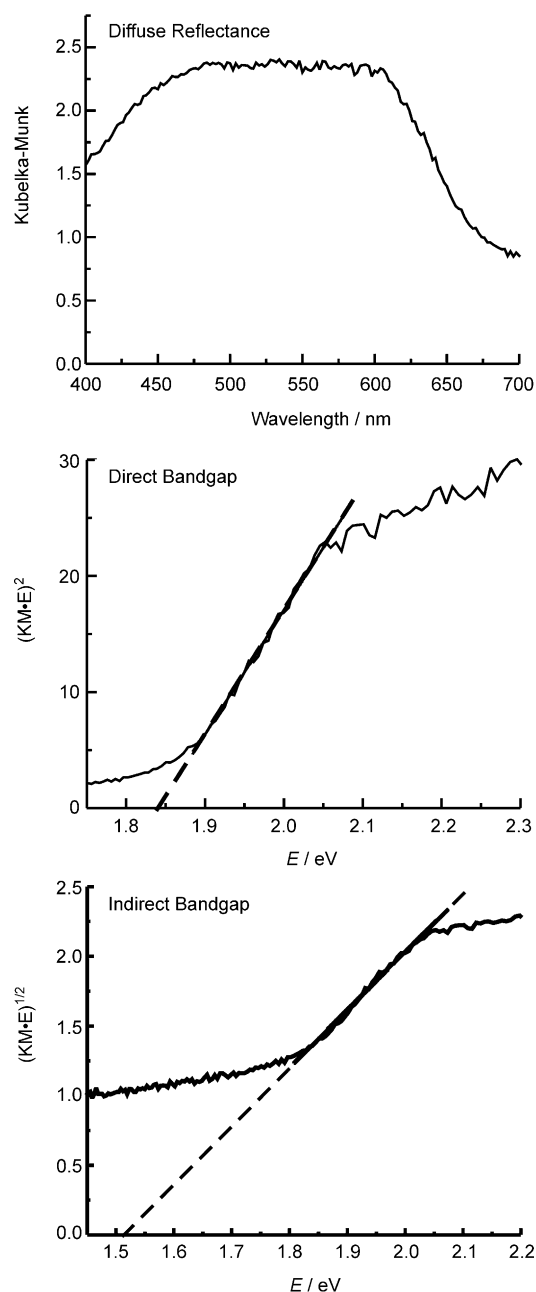


Figure 9. Solid-state UV/Vis spectra of $mP\text{-BaP}_3$: Kubelka–Munk diffuse reflectance (top); T_{auc} plots for allowed direct (middle) and indirect (bottom) transitions.

Conclusion

The synthesis, chemical features, and physical properties of a new polyphosphide $mP\text{-BaP}_3$ were explored and compared to those of the known polymorphic modification $mS\text{-BaP}_3$. The crystal structure of $mP\text{-BaP}_3$ contains a unique phosphorus polyanion, $\infty^2(\text{P}_3^{2-})$. According to the synthesis, differential scanning calorimetry, and quantum-mechanical calculations, $mP\text{-BaP}_3$ is a thermodynamically stable phase. ^{31}P solid-state NMR spectroscopy, calculations, as well as experimental determination of the bandgap indicate the importance of the weak Ba–P interactions for the electronic properties of the two

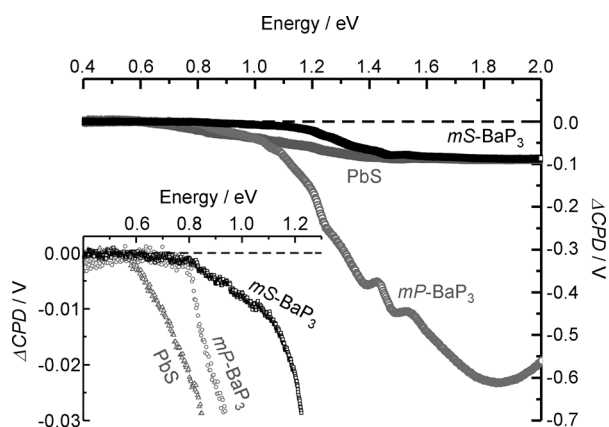


Figure 10. Surface photovoltage spectra for $mP\text{-BaP}_3$ (\circ), $mS\text{-BaP}_3$ (\blacksquare), and the PbS reference material (∇). Inset shows an enlarged part of the small ΔCPD range.

modifications of barium triphosphide. Both modifications of BaP_3 are semiconducting Zintl phases with considerably different bandgaps. This discovery of a new polyphosphide in the well-studied Ba–P binary system demonstrates the high versatility of phosphorus in forming various polyanionic fragments. It is expected that more binary phosphides are to be discovered.

Experimental Section

Synthesis

Single-phase samples of $mS\text{-BaP}_3$ and nearly pure samples of $mP\text{-BaP}_3$ were prepared by solid-state reactions in carbonized silica ampoules. The samples were assembled inside an argon-filled glovebox in which $p(\text{O}_2) < 1$ ppm. The starting materials were metallic barium (Sigma–Aldrich, 99.9%) and red phosphorus (Alfa Aesar, 99%), which were used as received. For both phases, the reactants were mixed in a stoichiometric ratio, placed in carbonized silica ampoules, evacuated, and flame-sealed. These reactions were found to be highly temperature sensitive and possibly pressure sensitive. Therefore, changing the ampoules' volume or the starting mass of reactants, affected the product composition. The final reactions were performed with a total reactant mass of 200 mg in a silica ampoule of 75 mm in length and 9 mm in inner diameter. The samples were ramped over 17 h to their final annealing temperature, 1073 K for $mP\text{-BaP}_3$ and 1173 K for $mS\text{-BaP}_3$, then they were annealed for 140 h, and finally they were cooled to room temperature. In the process of synthesis optimization, the samples were additionally annealed at 523 K overnight to prevent the ignition of traces of white phosphorus upon exposure to air.

X-ray powder diffraction and elemental analysis

A Bruker D8 Advance powder X-ray diffractometer with $\text{Cu}_{K\alpha}$ radiation was used (see Figure S1 in the Supporting Information). A Hitachi S4100T SEM with an energy-dispersive X-ray (EDX) microanalysis add-on (Oxford INCA energy) was used for the elemental analysis of the samples. EDX confirmed the presence of only Ba and P in both the $mP\text{-BaP}_3$ and $mS\text{-BaP}_3$ samples (see Figure S2 in the Supporting Information).

Single-crystal diffraction

A Bruker AXS Smart Diffractometer with an APEX II CCD Detector and $\text{Mo}_{K\alpha}$ radiation was used to characterize the single crystals. The datasets were integrated by using the Bruker SAINT software package, with multiscan absorption correction (SADABS). The crystal structures were solved and refined by using the SHELX suite of software.^[43] A summary of all important crystal structural information for the $mP\text{-BaP}_3$ and $mS\text{-BaP}_3$ phases can be found in Table 3.

Table 3. Data collection and crystal structure refinement parameters for $mP\text{-BaP}_3$ and $mS\text{-BaP}_3$.

Parameter	$mP\text{-BaP}_3$	$mS\text{-BaP}_3$
CSD-number	426770	426771
space group	$P2_1/c$ (no. 14)	$C2/m$ (no. 12)
T [K]	90(2)	90(2)
λ [Å]	0.71073	0.71073
a [Å]	6.4859(13)	11.627(2)
b [Å]	7.7105(15)	7.6529(15)
c [Å]	8.1719(16)	4.7469(9)
β [°]	104.72(3)	112.73(3)
V [Å ³]	395.26(13)	389.59(13)
Z	4	4
ρ [g cm ⁻³]	3.869	3.926
μ [mm ⁻¹]	11.011	11.171
θ [°]	$3.25 < \theta < 30.66$	$3.27 < \theta < 30.64$
data/parameters	1217/39	639/22
R_1	0.012	0.016
wR_2	0.028	0.041
goodness-of-fit	1.31	1.15
diff. peak and hole, [e/Å ³]	0.83, -0.40	1.67, -1.41

More information can be obtained from Fachinformationszentrum Karlsruhe, 76344 Eggenstein-Leopoldshafen, Germany, by quoting the depository CSD numbers.

Differential scanning calorimetry

A Netzsch differential scanning calorimeter (DSC) was used to characterize the thermal behavior of both phases. To maintain similar conditions to those of actual syntheses, DSC measurements were run by using small evacuated and sealed silica ampoules with enough sample to cover the base of the ampoule (approximately 30–50 mg). The samples were initially heated to 673 K at a rate of 10 Kmin⁻¹, and then the heating was slowed to 5 Kmin⁻¹ over the 673–1273 K range. A similar cooling scheme was employed. Each modification was tested several times to ensure reproducibility. Errors in the melting and crystallization temperatures are estimated not to exceed ± 3 K. Powder X-ray diffraction was subsequently used to determine the products of DSC thermal treatment.

UV/Vis diffuse reflectance

The experimental UV/Vis diffuse reflectance spectra were measured by using a Thermo Scientific Evolution 220 Spectrometer, and these data were used to calculate the Tauc plots. The solid samples were ground into powders and firmly pressed onto rough filter papers with a mechanical press. This formed a thick layer of compacted samples that could be measured without needing to suspend samples in solvent.

Surface photovoltage spectroscopy

Surface photovoltage spectra were recorded by using a Kelvin probe and controller (Delta Phi Besocke) connecting to a multimeter (Keithley 2700) for data measurement, a custom-built high-vacuum measurement chamber powered by a Pfeiffer HiCube 80 Eco turbo pump for the preferred vacuum conditions, and a 175 W Xe arc lamp (PE175-BF) in conjunction with a monochromator (Oriel Cornerstone 130) as the monochromatic light source. Samples were dispersed in acetone, dropcoated onto gold substrates and dried in air prior to being mounted inside the vacuum chamber. The Kelvin probe (Au grid, 3 mm diameter, 60% transparent) was placed 1.0 mm above the sample, and the chamber was evacuated to 10^{-7} bar for the measurements. Photovoltage spectra were obtained by scanning from low to high photon energy in 25 cm^{-1} steps with a period interval of 5 s per step. Raw light spectra were corrected for background effects (drift, desorption of gas and solvent molecules) by subtracting a linear signal drift. The sign convention is chosen so that a negative ΔCPD value will correspond to dipole with a positive pole at the surface and the negative side toward the gold substrate.

Solid-state ^{31}P NMR spectroscopy

The ^{31}P magic angle spinning (MAS) NMR spectra of polycrystalline samples were collected by using a Bruker Avance 500 spectrometer operating at a magnetic field of 11.7 T (^{31}P resonance frequency = 202.4 MHz) and a Bruker 2.5 mm MAS probe. Crushed BaP_3 samples were placed in ZrO_2 rotor and spun at frequencies ranging between 13 and 30 kHz. The one-pulse ^{31}P MAS NMR spectra were collected for each sample at 3 different spinning speeds, using a $\pi/4$ pulse (1 μs) and a recycle delay of 180 s. A total of 48 free induction decays were averaged and Fourier transformed to obtain each spectrum. The ^{31}P chemical shift was externally referenced to that of aqueous 85% H_3PO_4 .

Quantum-chemical calculations

Density-functional band structure calculations using a full potential all-electron local orbital code FPLO (version fplo7.00–28) within the local density approximation (LDA) were performed.^[44] The Perdew–Wang parameterization of the exchange–correlation potentials was employed.^[45] The density of states (DOS) and band structures were calculated after the convergence of the total energy on a dense k -mesh of $24 \times 24 \times 24$ points with 3770 ($m\text{P-BaP}_3$) and 3614 ($m\text{S-BaP}_3$) irreducible k -points. Additionally, electronic structure calculations and bonding analyses were carried out using the tight binding-linear muffin tin orbitals-atomic sphere approximation (TB-LMTO-ASA) program package.^[46] The Barth–Hedin exchange potential was employed for LDA calculations.^[47] The radial scalar-relativistic Dirac equation was solved to obtain the partial waves. A basis set containing $\text{Ba}(6s,5d,4f)$ and $\text{P}(3s,3p)$ orbitals was employed for a self-consistent calculation, with downfolding of $\text{Ba}(6p)$ and $\text{P}(3d)$ functions. The electron localization function (ELF, η)^[48] was evaluated with modules implemented within the TB-LMTO-ASA program package. The ParaView program was used for visualization of ELF isosurfaces.^[49]

Acknowledgements

We would like to thank to Prof. Dr. S. M. Kauzlarich for the access to DSC and K. Lee for the help with resistivity measurements. This research is supported by the U.S. Department of

Energy, Office of Basic Energy Sciences, Division of Materials Sciences and Engineering under Award DE-SC0008931.

Keywords: crystal structure · electronic structure · polyphosphide · solid-state NMR spectroscopy · zintl phases

- [1] H. G. Von Schnering, W. Höhle, *Chem. Rev.* **1988**, *88*, 243–273.
- [2] R. Pöttgen, W. Höhle, H. G. von Schnering, *Encyclopedia of Inorganic Chemistry*, 2nd ed., King, R. B., Ed., Wiley, Chichester, U. K., **2005**, *8*, 4255–4308.
- [3] M. M. Shatruk, K. A. Kovnir, A. V. Shevelkov, B. A. Popovkin, *Angew. Chem.* **2000**, *112*, 2561–2562; *Angew. Chem. Int. Ed.* **2000**, *39*, 2508–2509.
- [4] a) T. F. Fässler, *Struct. Bonding (Berlin)* **2011**, *140*, 91–131; b) S. Scharfe, F. Kraus, S. Stegmaier, A. Schier, T. F. Fassler, *Angew. Chem.* **2011**, *123*, 3712–3754; *Angew. Chem. Int. Ed.* **2011**, *50*, 3630–3670.
- [5] a) S. Lange, C. P. Sebastian, L. Zhang, H. Eckert, T. Nilges, *Inorg. Chem.* **2006**, *45*, 5878–5885; b) S. Lange, C. P. Sebastian, T. Nilges, *Z. Anorg. Allgem. Chem.* **2006**, *632*, 195–203; c) S. Lange, T. Nilges, *Z. Naturforsch. B* **2006**, *61*, 871–881; d) S. Lange, M. Bawohl, R. Wehrich, T. Nilges, *Angew. Chem.* **2008**, *120*, 5736–5739; *Angew. Chem. Int. Ed.* **2008**, *47*, 5654–5657; e) H. Lincke, T. Nilges, D. Johrendt, R. Pöttgen, *Solid State Sci.* **2008**, *10*, 1006–1011; f) M. Bawohl, T. Nilges, *Z. Anorg. Allgem. Chem.* **2009**, *635*, 307–311; g) M. Bawohl, T. Nilges, *Z. Anorg. Allgem. Chem.* **2009**, *635*, 667–673; h) R. Wehrich, S. Lange, T. Nilges, *Solid State Sci.* **2009**, *11*, 519–527; i) M. Bawohl, P. Schmidt, T. Nilges, *Inorg. Chem.* **2013**, *52*, 11895–11901; j) N. Eckstein, A. Hohmann, R. Wehrich, T. Nilges, P. Schmidt, *Z. Anorg. Allgem. Chem.* **2013**, *639*, 2741–2743.
- [6] a) M. V. Dewalsky, W. Jeitschko, U. Wortmann, *Chem. Mater.* **1991**, *3*, 316–319; b) M. Eschen, J. Wallinda, W. Jeitschko, *Z. Anorg. Allgem. Chem.* **2002**, *628*, 2764–2771; c) P. Kaiser, W. Jeitschko, *Z. Anorg. Allgem. Chem.* **1996**, *622*, 53–56; d) M. Eschen, W. Jeitschko, *J. Solid State Chem.* **2002**, *165*, 238–246; e) T. Bartsch, T. Wiegand, J. Ren, H. Eckert, D. Johrendt, O. Niehaus, M. Eul, R. Pöttgen, *Inorg. Chem.* **2013**, *52*, 2094–2102; f) M. Eul, M. H. Möller, R.-D. Hoffmann, W. Jeitschko, R. Pöttgen, *Z. Anorg. Allg. Chem.* **2012**, *638*, 331–335; g) U. Pfannenschmidt, F. Behrends, H. Lincke, M. Eul, K. Schäfer, H. Eckert, R. Pöttgen, *Dalton Trans.* **2012**, *41*, 14188–14196.
- [7] B. Eisenmann, U. Rößler, *Z. Anorg. Allgem. Chem.* **2003**, *629*, 459–462.
- [8] X. Chen, L.-P. Zhu, S. Yamanaka, *J. Solid State Chem.* **2003**, *173*, 449–455.
- [9] a) A. S. Ivanov, A. J. Morris, K. V. Bozhenko, C. J. Pickard, A. I. Boldyrev, *Angew. Chem.* **2012**, *124*, 8455–8458; *Angew. Chem. Int. Ed.* **2012**, *51*, 8330–8333; b) A. S. Ivanov, A. I. Boldyrev, G. Frenking, *Chem. Eur. J.* **2014**, *20*, 2431–2435.
- [10] J. Dünner, A. Mewis, *Z. Anorg. Allg. Chem.* **1995**, *621*, 191–196.
- [11] K. Kovnir, U. Stockert, S. Budnyk, Y. Prots, M. Baitinger, S. Paschen, A. V. Shevelkov, Y. Grin, *Inorg. Chem.* **2011**, *50*, 10387–10396.
- [12] W. Dahlmann, H. G. von Schnering, *Naturwissenschaften* **1973**, *60*, 518–518.
- [13] C. Hadenfeldt, *Z. Anorg. Allg. Chem.* **1977**, *436*, 113–121.
- [14] C. Hadenfeldt, H.-U. Terschüren, W. Höhle, L. Schröder, H. G. Von Schnering, *Z. Anorg. Allg. Chem.* **1993**, *619*, 843–848.
- [15] G. Derrien, M. Tillard, A. Manteghetti, C. Belin, *Z. Anorg. Allg. Chem.* **2003**, *629*, 1601–1609.
- [16] H.-G. von Schnering, M. Wittmann, D. Sommer, *Z. Anorg. Allg. Chem.* **1984**, *510*, 61–71.
- [17] BaP_2 : $P2_1/n$: $a=6.3705(7)$, $b=12.142(1)$, $c=6.4125(8)$ Å, $\beta=106.018(2)^\circ$, $R_1=0.014$, $wR_2=0.029$.
- [18] H. G. von Schnering, W. Dahlmann, *Naturwissenschaften* **1971**, *58*, 623–624.
- [19] W. Dahlmann, H. G. Schnering, *Naturwissenschaften* **1973**, *60*, 429–429.
- [20] H. G. von Schnering, G. Menge, *Z. Anorg. Allg. Chem.* **1982**, *491*, 286–294.
- [21] J. Fulmer, D. C. Kaseman, J.-A. Dolyniuk, K. Lee, S. Sen, K. Kovnir, *Inorg. Chem.* **2013**, *52*, 7061–7067.
- [22] J. Fulmer, O. I. Lebedev, V. V. Roddatis, D. C. Kaseman, S. Sen, J.-A. Dolyniuk, K. Lee, A. V. Olenev, K. Kovnir, *J. Am. Chem. Soc.* **2013**, *135*, 12313–12323.

- [23] J.-A. Dolyniuk, K. Kovnir, *Crystals* **2013**, *3*, 431–442.
- [24] T. Meyer, W. Höhle, H. G. von Schnering, *Z. Anorg. Allg. Chem.* **1987**, *552*, 69–80.
- [25] H. P. Abicht, W. Höhle, H. G. v. Schnering, *Z. Anorg. Allg. Chem.* **1984**, *519*, 7–23.
- [26] H. G. von Schnering, M. Somer, G. Kliche, W. Höhle, T. Meyer, J. Wolf, L. Ohse, P. B. Kempa, *Z. Anorg. Allg. Chem.* **1991**, *601*, 13–30.
- [27] H. Krebs, K. H. Müller, G. Zürn, *Z. Anorg. Allg. Chem.* **1956**, *285*, 15–28.
- [28] D. Massiot, F. Fayon, M. Capron, I. King, S. Le Calvé, B. Alonso, J.-O. Durand, B. Bujoli, Z. Gan, G. Hoatson, *Magn. Reson. Chem.* **2002**, *40*, 70.
- [29] J. S. auf der Günne, S. Kaczmarek, L. van Wullen, H. Eckert, D. Paschke, A. J. Foecker, W. Jeitschko, *J. Solid State Chem.* **1999**, *147*, 341.
- [30] S. M. Kauzlarich, *Chemistry, structure, and bonding of Zintl phases and ions*, VCH, Weinheim, **1996**.
- [31] G. J. Miller, M. W. Schmidt, F. Wang, T. S. You, *Struct. Bonding (Berlin)* **2011**, *139*, 1–55.
- [32] A. B. Murphy, *Sol. Energy Mater. Sol. Cells* **2007**, *91*, 1326–1337.
- [33] T. K. Townsend, N. D. Browning, F. E. Osterloh, *ACS Nano* **2012**, *6*, 7420–7426.
- [34] L. Kronik, Y. Shapira, *Surf. Sci. Rep.* **1999**, *37*, 1–206.
- [35] L. Kronik, Y. Shapira, *Surf. Interface Anal.* **2001**, *31*, 954–965.
- [36] T. K. Townsend, N. D. Browning, F. E. Osterloh, *Energy Environ. Sci.* **2012**, *5*, 9543–9550.
- [37] M. Waller, T. K. Townsend, J. Zhao, E. M. Sabio, R. L. Chamousis, N. D. Browning, F. E. Osterloh, *Chem. Mater.* **2012**, *24*, 698–704.
- [38] D. Gross, I. Mora-Sero, T. Dittrich, A. Belaidi, C. Mauser, A. J. Houtepen, E. Da Como, A. L. Rogach, J. Feldmann, *J. Am. Chem. Soc.* **2010**, *132*, 5981–5983; Mauser, A. J. Houtepen, E. Da Como, A. L. Rogach, J. Feldmann, *J. Am. Chem. Soc.* **2010**, *132*, 5981–5983.
- [39] T. Dittrich, S. Fiechter, A. Thomas, *Appl. Phys. Lett.* **2011**, *99*, 084105.
- [40] a) F. E. Osterloh, M. A. Holmes, L. Chang, A. J. Moule, J. Zhao, *J. Phys. Chem. C* **2013**, *117*, 26905–26913; b) J. Zhao, F. E. Osterloh, *J. Phys. Chem. Lett.* **2014**, *5*, 782–786.
- [41] O. Madelung, *Semiconductors: Data Handbook*, 3rd ed., Springer, Heidelberg, **2004**, p. 691.
- [42] A. Osherov, J. P. Makai, J. Balazs, Z. J. Horvath, N. Gutman, A. Sa'ar, Y. Golan, *J. Phys. Condens. Matter* **2010**, *22*, 262002.
- [43] G. M. Sheldrick, *Acta Crystallogr. Sect. A* **2008**, *64*, 112–122.
- [44] a) K. Koepernik, H. Eschrig, *Phys. Rev. B* **1999**, *59*, 1743. b) I. Ophale, K. Koepernik, H. Eschrig, *Phys. Rev. B* **2000**, *60*, 14035.
- [45] J. P. Perdew, Y. Wang, *Phys. Rev. B* **1992**, *45*, 13244.
- [46] O. Jepsen, A. Burkhardt, O. K. Andersen, *The Program TBLMTO-ASA*, Version 4.7, Max-Planck-Institut für Festkörperforschung, Stuttgart, Germany, **1999**.
- [47] U. von Barth, L. Hedin, *J. Phys. C* **1972**, *5*, 1629–1642.
- [48] a) A. D. Becke, K. E. Edgecombe, *J. Chem. Phys.* **1990**, *92*, 5397–5403; b) A. Savin, O. Jepsen, J. Flad, O. K. Andersen, H. Preuss, H. G. von Schnering, *Angew. Chem.* **1992**, *104*, 186–188; *Angew. Chem. Int. Ed. Engl.* **1992**, *31*, 187–188; c) A. Savin, R. Nesper, S. Wengert, T. F. Fassler, *Angew. Chem.* **1997**, *109*, 1892–1918; *Angew. Chem. Int. Ed. Engl.* **1997**, *36*, 1808–1832.
- [49] a) Paraview: Parallel visualization application, version 3.8.1 64 bit; Sandia National Labs, Kitware Inc, Los Alamos National Labs: USA; <http://paraview.org>; b) A. I. Baranov, *Visualization plugin for ParaView*, Version 3.4.11, 2012. 1.

 Received: December 30, 2013

Revised: April 8, 2014

Published online on May 21, 2014